Lin Gong, Pete Hollings, Yu Zhang, Jing Tian, Dengfeng Li, Al Emil Berador, and Huayong Chen, 2020, Contribution of an Eastern Indochina-derived fragment to the formation of island arc systems in the Philippine Mobile Belt: GSA Bulletin, https://doi.org/10.1130/B35793.1.

Supplemental Material

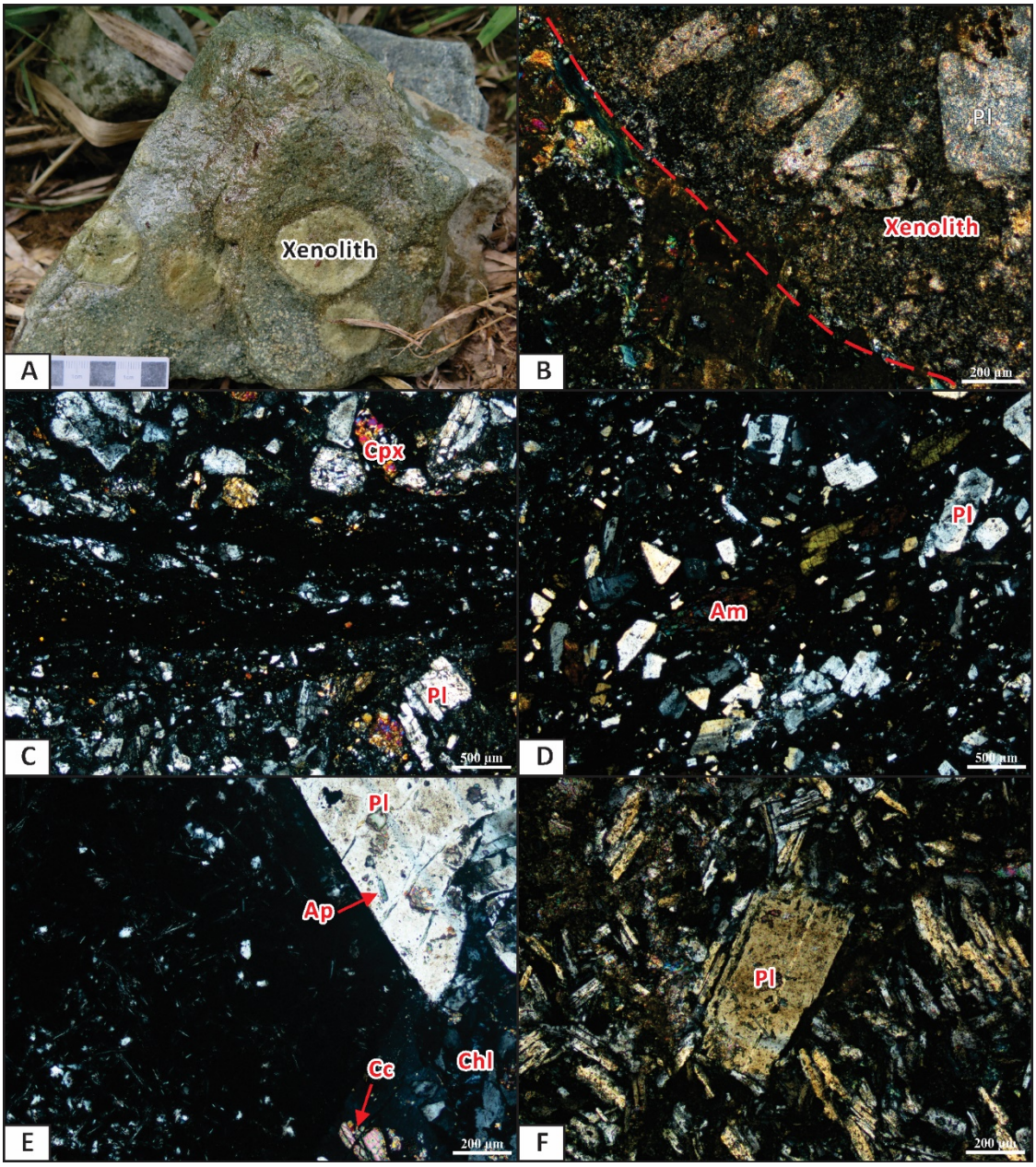

Figure S1-1. Representative field photographs and Photomicrographs for the Cretaceous igneous rocks. (**A**) Pyroxene andesite with crustal xenoliths (sample C9-2). (**B**) Photomicrograph (in CPL) showing the contact between the pyroxene andesite and xenoliths, the xenoliths mainly consist of plagioclase phenocrysts in a matrix of fine-grained plagioclase and aphanitic crystals, plagioclase phenocrysts are strongly altered to sericite. (**C**) Plain polarized (PPL) photomicrographs showing basaltic-andesitic crystal fragment tuff with pseudo fluxion structure and the crystal fragments are mainly composed of clinopyroxene and plagioclase. (**D**) Photomicrograph of andesitic crystal fragment tuff and its crystal fragments consist of plagioclase and hornblende (in CPL). (**E**) cross polarized (CPL) photomicrographs showing andesite with coarse plagioclase phenocrysts in a

glassy matrix. (**F**) Andesite with plagioclase phenocrysts in groundmass of fine-grained feldspars and aphanitic crystals (in CPL).

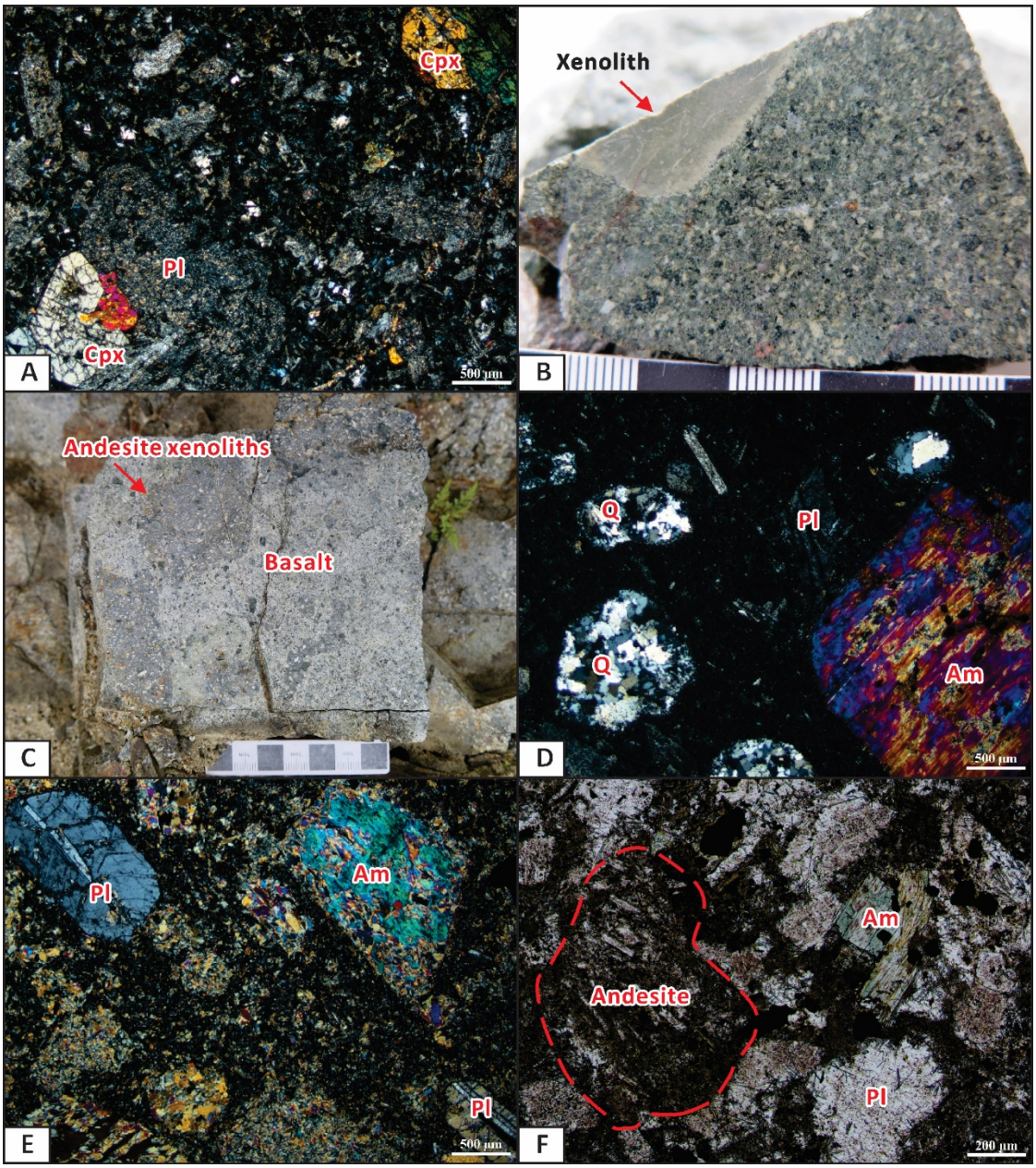

Figure S1-2. Representative field photographs and Photomicrographs for the Paleogene igneous rocks. (**A**) Photomicrographs showing basaltic andesite with plagioclase and clinopyroxene phenocrysts in matrix of fine-grained feldspar, clinopyroxene and Fe-Ti oxide (in CPL). (**B**) Cut surface (sample C19-8) showing andesitic crystal fragment tuff with crustal xenoliths. (**C**) Outcrop of andesite xenoliths in basalt. (**D**) Photomicrograph showing andesite with amphibole and plagioclase phenocrysts in matrix of microcrystalline plagioclase, amphibole and Fe-Ti oxide, quartz polycrystalline aggregate are also observed (in CPL). (**E**) Cross polarized photomicrograph showing plagioclase and clinopyroxene phenocrysts, clinopyroxene phenocrysts are entirely

altered into amphibole. (**F**) Plain polarized photomicrograph showing andesitic lithic crystal tuff consisting of andesite debris, plagioclase and amphibole crystal fragments (sample B14)

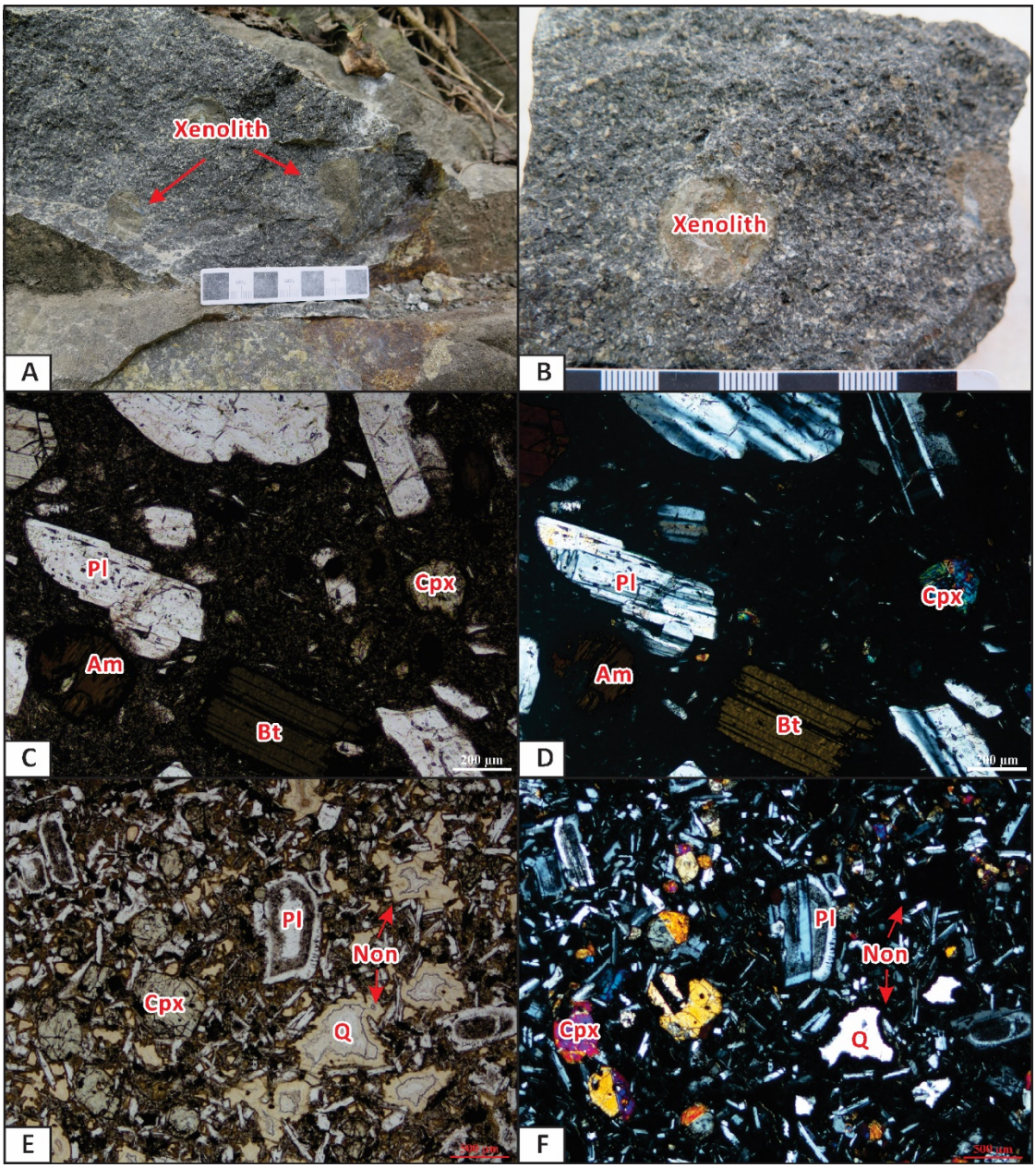

Figure S1-3. Representative field photographs and Photomicrographs for the Middle Miocene andesite. (**A**) Outcrop of andesite with crustal xenoliths. (**B**) Specimen of andesite with crustal xenoliths. (**C-D**) Photomicrographs showing andesite with plagioclase, clinopyroxene, hornblende and biotite phenocrysts in matrix of microcrystalline feldspar, hornblende, pyroxene, Fe-Ti oxide and glassy minerals (left in PPL, right in CPL). (**E-F**) Photomicrographs showing xenoliths with plagioclase and clinopyroxene phenocrysts in matrix of microcrystalline feldspar, pyroxene, Fe-Ti oxide and glassy minerals, abundant quartz and nontronite amygdala can be also identified (left in PPL, right in CPL).

Mineral abbreviations: Cpx—clinopyroxene, Am—amphibole, Bt—biotite, Pl—plagioclase, Q—quartz, Ap—apatite, Chl—chlorite, Cc—calcite, Non—nontronite.

Figure S2. Cathodoluminescence images of representative zircons for U-Pb dating and Lu-Hf isotope analyses for igneous rocks from Cebu and Bohol islands.

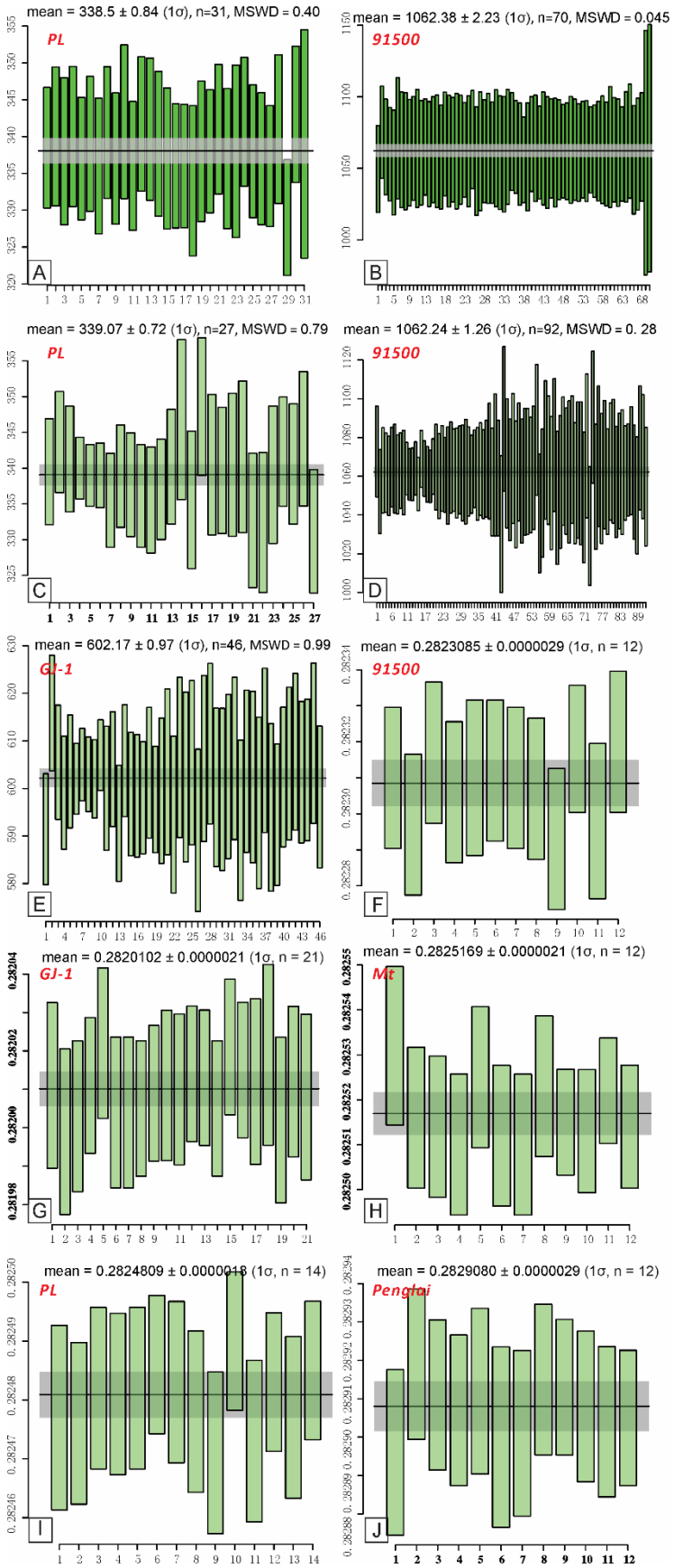
mean = 338.5 ± 0.84 (1σ), n=31, MSWD = 0.40
PL
A
mean = 1062.38 ± 2.23 (1σ), n=70, MSWD = 0.045
91500
B
mean = 339.07 ± 0.72 (1σ), n=27, MSWD = 0.79
PL
C
mean = 1062.24 ± 1.26 (1σ), n=92, MSWD = 0. 28
91500
D
mean = 602.17 ± 0.97 (1σ), n=46, MSWD = 0.99
GJ-1
E
mean = 0.2823085 ± 0.0000029 (1σ, n = 12)
91500
F
mean = 0.2820102 ± 0.0000021 (1σ, n = 21)
GJ-1
G
mean = 0.2825169 ± 0.0000021 (1σ, n = 12)
Mt
H
mean = 0.2824809 ± 0.0000018 (1σ, n = 14)
PL
I
mean = 0.2829080 ± 0.0000029 (1σ, n = 12)
Penglai
J

Figure S3. Weighted mean $^{206}Pb/^{238}U$ ages for 91500, Plešovice (PL), GJ-1 zircon standards and weighted mean $^{176}Hf/^{177}Hf$ ratios for GJ-1, 91500, Plešovice (PL), Mud Tank (Mt), Penglai zircon standards (see below).

Note: The results of zircon age standards employed at SYU are presented in Figs. S3A-B, while the results of standards used at Nanjing FocuMS Technology Co. Ltd. are shown in Figs. S3C-E. The remaining figures are for $^{176}Hf/^{177}Hf$ ratios of zircon standards measured at Nanjing FocuMS Technology Co. Ltd.

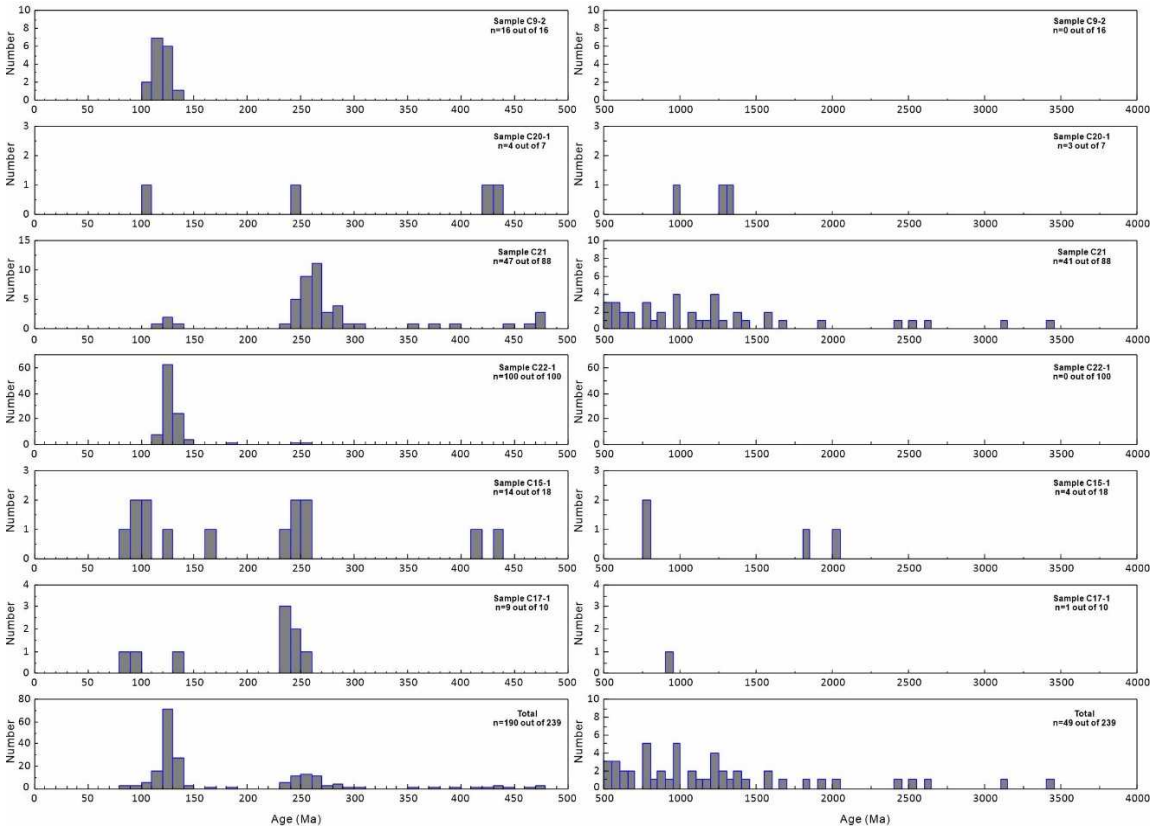

Figure S4-1. Zircon U-Pb age distribution of each sample for magmatic rocks in the Cretaceous.

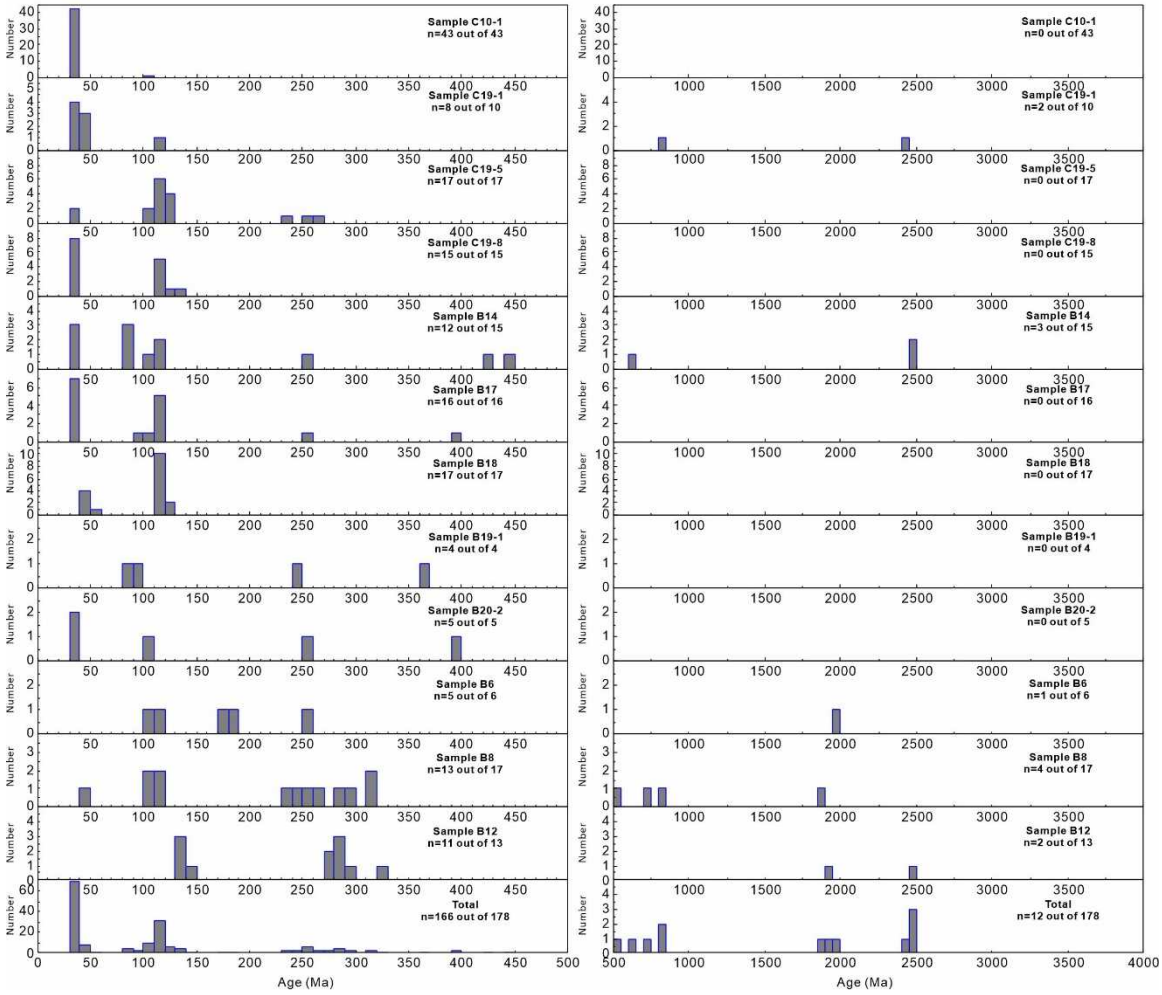

Figure S4-2. Zircon U-Pb age distribution of each sample for magmatic rocks in the Middle Eocene to Early Oligocene.

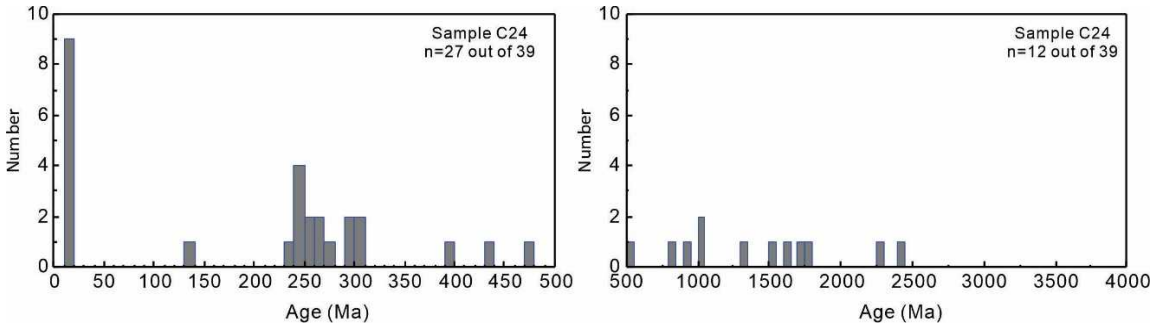

Figure S4-3. Zircon U-Pb age distribution of each sample for magmatic rocks in the Middle Miocene.

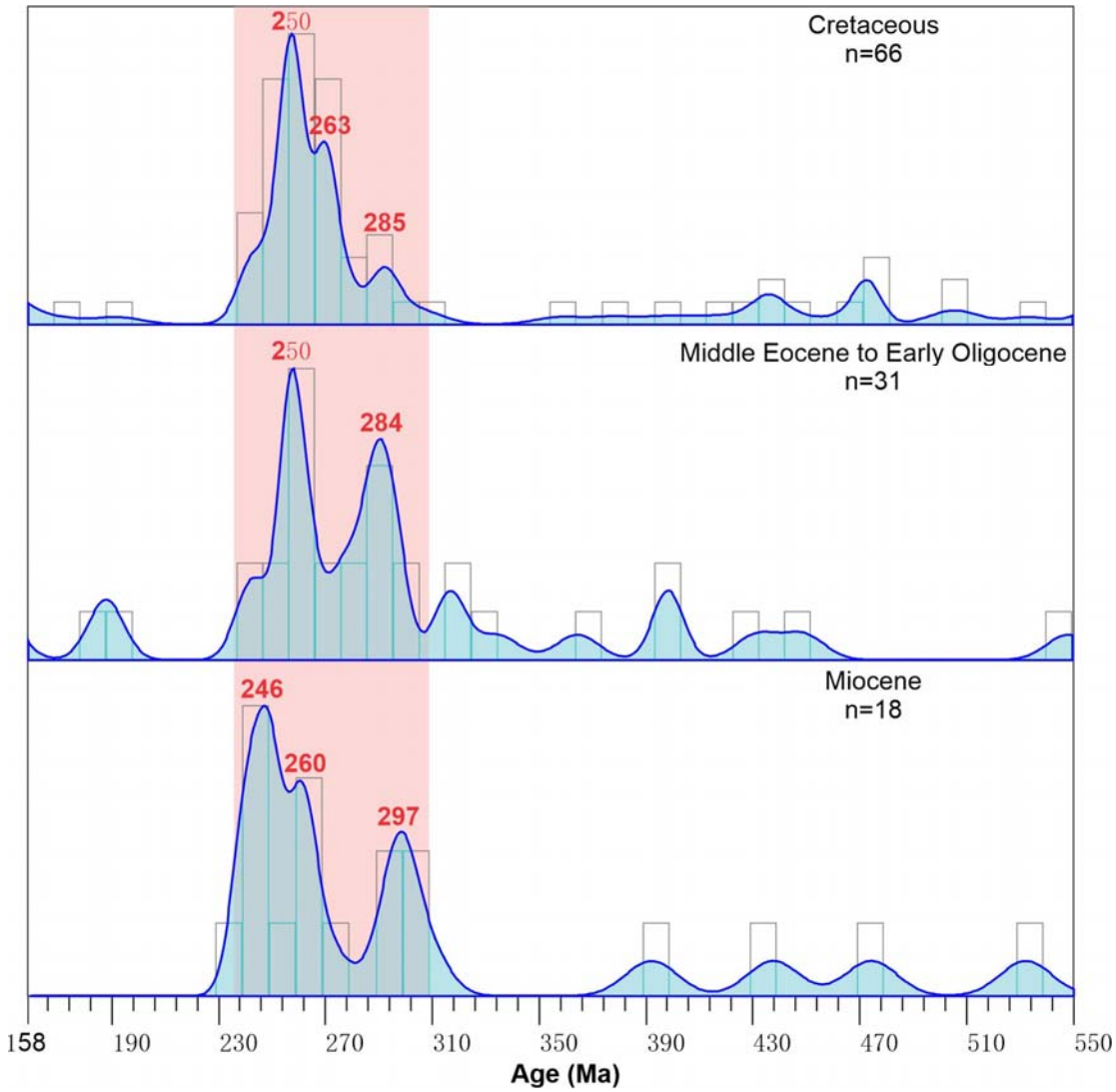

Figure S5. Relative probability density diagram of the inherited/xenocrystic zircons (550–160 Ma) from the Cebu and Bohol islands.

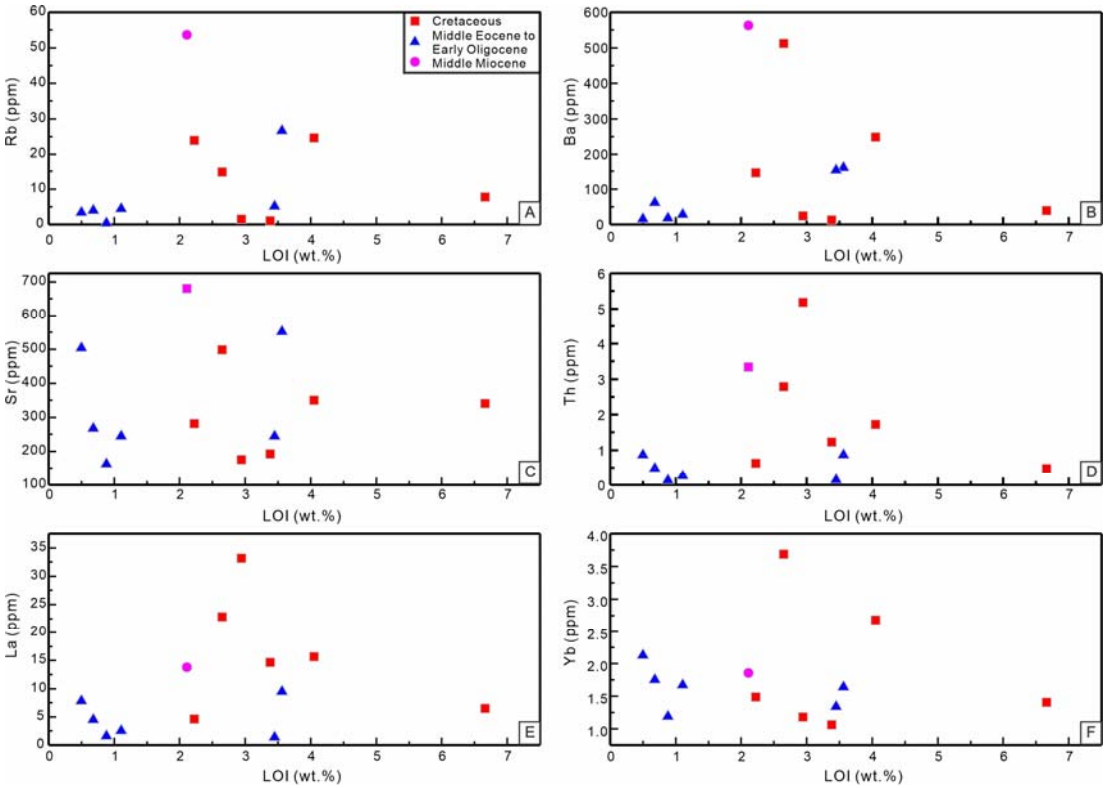

Figure S6. Diagram of loss-on-ignition (LOI) versus Rb, Ba, Sr, Th, La and Yb contents.

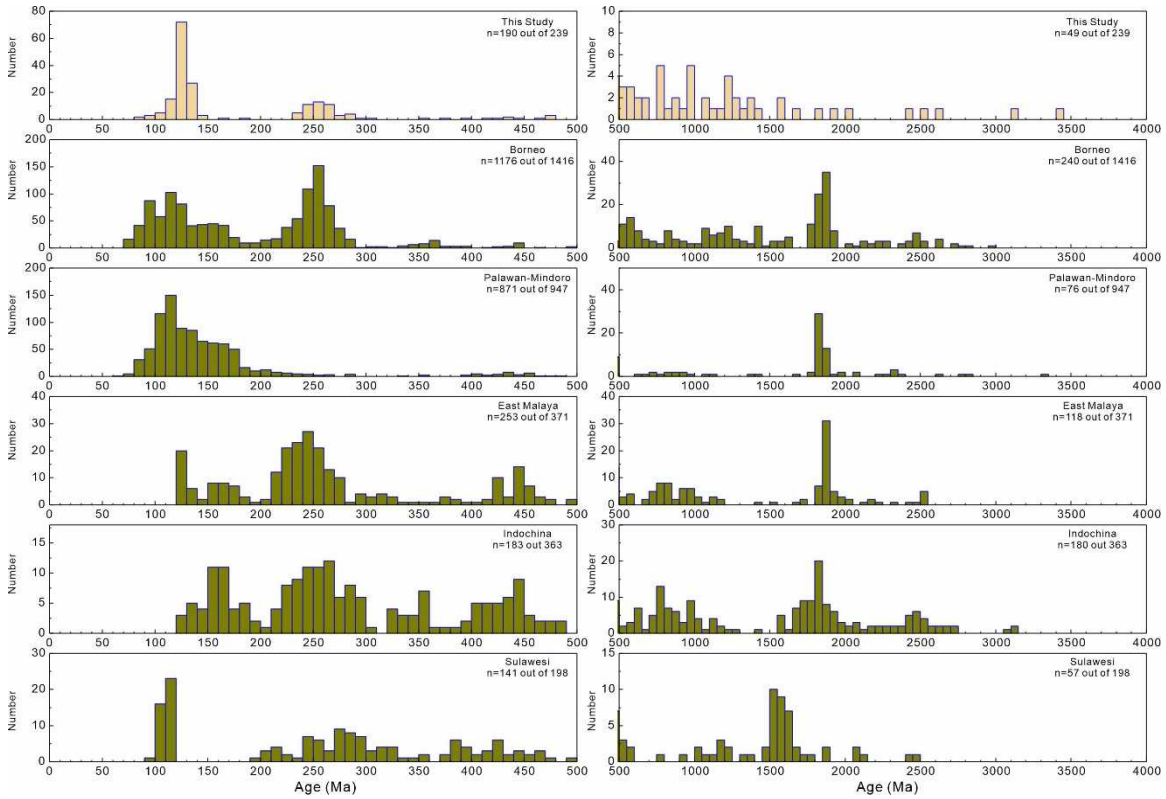

Figure S7-1. Zircon U-Pb age spectra for Cretaceous samples in this study and surrounding terranes including Borneo (Breitfeld and Hall, 2018; Breitfeld et al., 2017; Galin et al., 2017), Palawan-Mindoro (Shao et al., 2017; Suggate et al., 2014), East Malaya (Dodd et al., 2019), Indochina (Carter and Moss, 1999) and Sulawesi (Jaya et al., 2017).

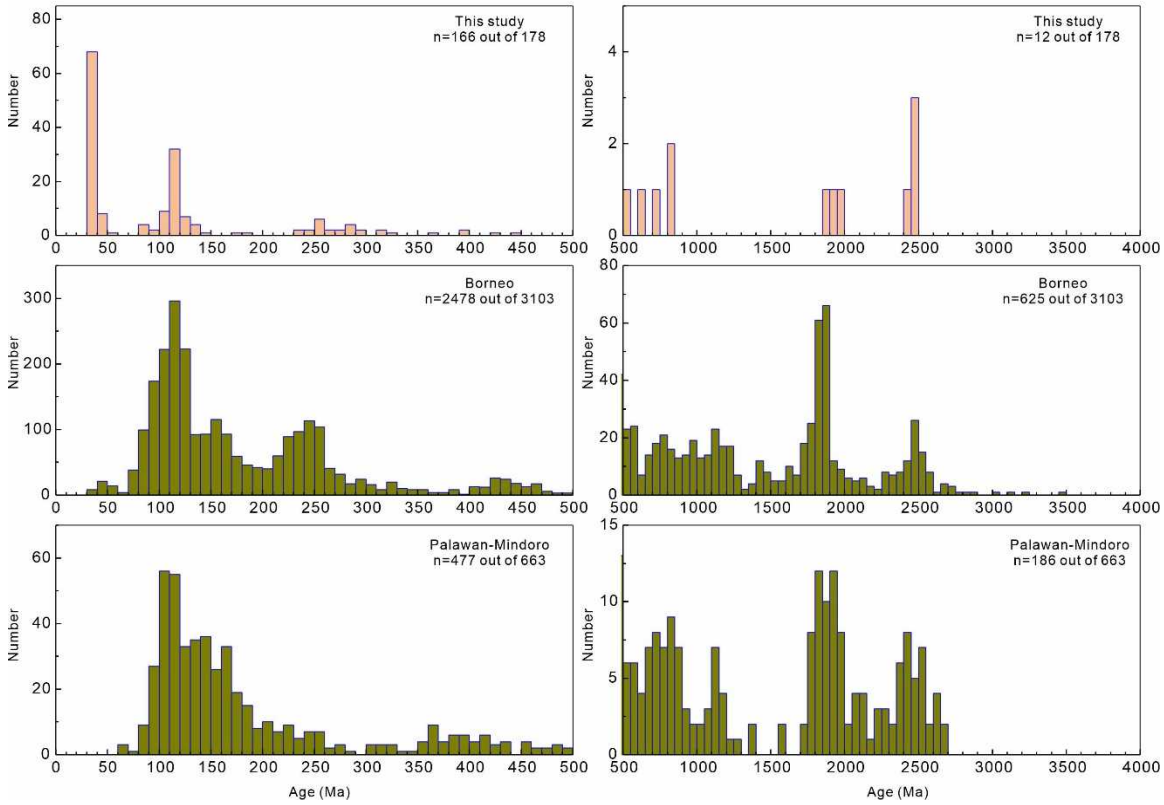

Figure S7-2. Zircon U-Pb age spectra for Eocene to Oligocene samples in this study and surrounding terranes including Borneo (Breitfeld and Hall, 2018; Galin et al., 2017; Hennig-Breitfeld et al., 2019; van Hattum et al., 2006) and Palawan-Mindoro (Shao et al., 2017; Yan et al., 2018).

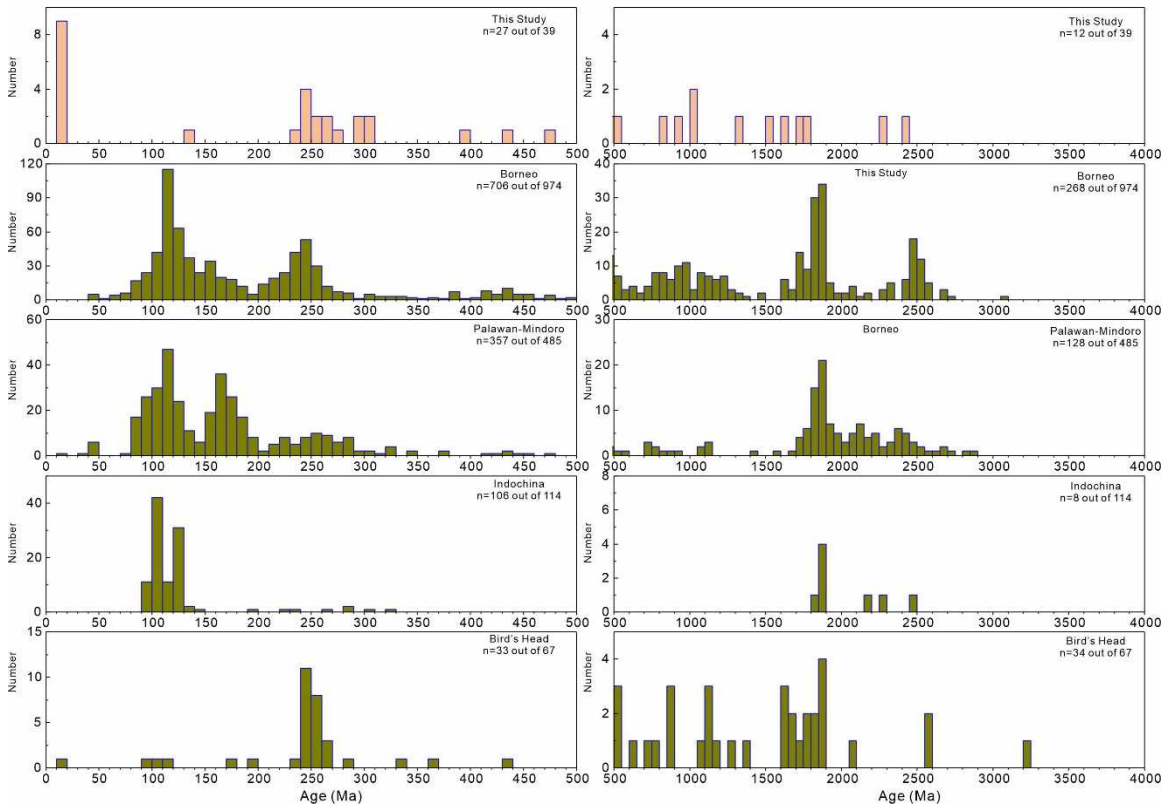

Figure S7-3. Zircon U-Pb age spectra for Middle Miocene sample in this study and surrounding terranes including Borneo (Hennig-Breitfeld et al., 2019), Palawan-Mindoro (Suggate et al., 2014; Yan et al., 2018), Indochina (Hennig et al., 2018) and Bird's Head (Webb et al., 2019).

Additional Supplementary tables (with files uploaded separately)

Table S1. Whole rock geochemical and Sr-Nd isotope data for igneous rocks from Cebu and Bohol islands

Table S2. U-Pb age data for zircons in igneous rocks from Cebu and Bohol islands

Table S3. Trace elements for zircons in igneous rocks from Cebu and Bohol islands

Table S4. Hafnium isotopic compositions for zircons in igneous rocks from Cebu and Bohol islands

$$\varepsilon Hf(t) = \left[\frac{\left(\frac{^{176}Hf}{^{177}Hf}\right)_{sample} - \left(\frac{^{176}Lu}{^{177}Hf}\right)_{sample} \times (e^{\lambda t} - 1)}{\left(\frac{^{176}Hf}{^{177}Hf}\right)_{CHUR} - \left(\frac{^{176}Lu}{^{177}Hf}\right)_{CHUR} \times (e^{\lambda t} - 1)} - 1\right] \times 104$$

$$T_{DM} = 1/\lambda \times \ln\left\{1 + \frac{\left(\frac{^{176}Hf}{^{177}Hf}\right)_{sample} - \left(\frac{^{176}Hf}{^{177}Hf}\right)_{DM}}{\left(\frac{^{176}Lu}{^{177}Hf}\right)_{sample} - \left(\frac{^{176}Lu}{^{177}Hf}\right)_{DM}}\right\}$$

$$T_{2DM} = T_{DM} - (T_{DM} - t) \times \frac{(f_{MC} - f_{Sample})}{(f_{MC} - f_{DM})}$$

$$f_{sample} = \frac{(^{176}Lu/^{177}Hf)_{Sample}}{(^{176}Lu/^{177}Hf)_{CHUR}} - 1;\ f_{MC} = \frac{(^{176}Lu/^{177}Hf)_{MC}}{(^{176}Lu/^{177}Hf)_{CHUR}} - 1;\ f_{DM} = \frac{(^{176}Lu/^{177}Hf)_{DM}}{(^{176}Lu/^{177}Hf)_{CHUR}} - 1.$$

$\lambda = 1.867 \times 10^{-11}$ yr^{-1} (Söderlund et al., 2004); $(^{176}Lu/^{177}Hf)_{CHUR} = 0.0332$, $(^{176}Hf/^{177}Hf)_{CHUR} = 0.282772$ (Blichert-Toft and Albarède, 1997); $(^{176}Lu/^{177}Hf)_{DM} = 0.0384$, $(^{176}Hf/^{177}Hf)_{DM} = 0.28325$, $(^{176}Lu/^{177}Hf)_{MC} = 0.015$ (Griffin et al., 2000; 2002).

t = crystallization time of zircon. $^{206}Pb/^{238}U$ and $^{207}Pb/^{206}Pb$ ages were used for zircons younger than 1000 Ma and older than 1000 Ma, respectively.

Table S5. Compiled zircon U-Pb age and Lu-Hf isotopic data